

5953 **Chapter 9**  
5954 **Strong Focusing Synchrotron**

5955 **Abstract** This Chapter introduces the strong focusing alternating gradient (AG)  
5956 and separated function synchrotrons. It provides the theoretical material which the  
5957 simulation exercises lean on. The chapter begins with a brief reminder of the histor-  
5958 ical context, and continues with beam optics, chromaticity, acceleration, resonances  
5959 and resonant extraction, dynamical effects of synchrotron radiation (SR), the elec-  
5960 tromagnetic SR impulse, and depolarizing resonances. This resorts to basic charged  
5961 particle optics, acceleration, and dynamics in magnetic fields introduced in the pre-  
5962 vious Chapters.

5963 The simulation of a strong focusing AG synchrotron requires just two optical el-  
5964 ements from `zgoubi` library: `DIPOLE` or `MULTIPOL` to simulate a combined  
5965 function dipole, and `DRIFT` to simulate straight sections. Main dipoles in a sep-  
5966 arated function synchrotron can use `BEND`. It requires in addition quadrupoles,  
5967 simulated using `QUADRUPO` or `MULTIPOL`. The latter can simulate higher order  
5968 lenses, which can otherwise resort to `SEXTUPOL`, `OCTUPOLE`, etc. Acceleration  
5969 uses `CAVITE`. Accounting for synchrotron radiation (SR) energy loss requires `SR-`  
5970 `LOSS`. Monte Carlo SR monitoring can use `SRPRNT`, which logs data in `zgoubi.res`.  
5971 `SRPRNT[PRINT]` in addition logs data in `zgoubi.SRPRNT.Out`. Computation of  
5972 synchrotron radiation (SR) Poynting and spectral brightness uses `zpop`. Particle  
5973 monitoring requires keywords introduced in the previous Chapters, including `FAIS-`  
5974 `CEAU`, `FAISTORE`, possibly `PICKUPS`, and some others. Spin motion computation  
5975 and monitoring resort to `SPNTRK`, `SPNPRT`, `FAISTORE`. Optics matching and op-  
5976 timization use `FIT[2]`. `INCLUDE` is used, mostly here in order to simplify the input  
5977 data files. `SYSTEM` is used to, mostly, resort to `gnuplot` so as to end simulations with  
5978 some specific graphs. Data for the latter are read from output files filled up during  
5979 the execution of the code, such as `zgoubi.fai` (resulting from the use of `FAISTORE`),  
5980 `zgoubi.plt` (resulting from `IL=2`), or other `zgoubi.*.out` files resulting from a `PRINT`  
5981 command. Stepwise particle data logged in `zgoubi.plt` are used by the interface `zpop`  
5982 to compute the electric field impulse of SR and subsequent spectral angular energy  
5983 density of the radiation.

5984 **Notations used in the Text**

$\mathbf{B}; B_{x,y,s}; B$	field vector; its components in the moving frame; its modulus
$B\rho = p/q; B\rho_0$	particle rigidity; reference rigidity
$C; C_0$	orbit length; $C = 2\pi R + \left[ \begin{smallmatrix} \text{straight} \\ \text{sections} \end{smallmatrix} \right]$ ; reference, $C_0 = C(p = p_0)$
$\mathbf{E}; E_\sigma, E_\pi$	SR electric field impulse; its parallel and normal components
$E; E_s$	particle energy, $E = \gamma m_0 c^2$ ; synchronous energy
EFB	Effective Field Boundary
$f_{\text{rev}}, f_{\text{rf}} = h f_{\text{rev}}$	revolution and RF voltage frequencies
$G$	gyromagnetic anomaly, $G = 1.792847$ for proton
$G; K = G/B\rho$	quadrupole gradient; focusing strength
$h$	RF harmonic number
$m; m_0; M$	particle mass; rest mass; in units of $\text{MeV}/c^2$
$n = -\frac{\rho}{B} \frac{\partial B}{\partial x}$	focusing index
$\mathbf{n}_0$	stable spin precession direction
$\mathbf{P} = \mathbf{E} \times \mathbf{B}$	SR Poynting vector
$P_i, P_f$	beam polarization, initial, final
$\mathbf{p}; p; p_0$	momentum vector; its modulus; reference
$q$	particle charge
$r; R$	orbital radius ; average radius, $R = C/2\pi$
$S$	periodicity of the lattice; or sextupole strength
$s$	path variable
$U_s$	SR energy loss
$\mathbf{v}; v$	particle velocity vector; its modulus
$V(t); \hat{V}$	oscillating voltage; its peak value
5985 $x, x', y, y', l, \frac{dp}{p}$	particle coordinates in the moving frame, $[(*)' = d(*)/ds]$
$\alpha$	momentum compaction; or trajectory deviation; or depolarizing resonance crossing speed
$\beta = v/c; \beta_0; \beta_s$	normalized particle velocity; reference; synchronous
$\beta_u$	betatron functions ( $u : x, y, Y, Z$ )
$\gamma = E/m_0 c^2$	Lorentz relativistic factor
$\gamma_{\text{tr}}$	transition $\gamma$ , $\gamma_{\text{tr}} = 1/\sqrt{\alpha}$
$\delta p, \Delta p$	momentum offset
$\epsilon_c$	critical energy of SR, $\epsilon_c = \hbar\omega_c = hc/\lambda_c$
$\varepsilon$	wedge angle
$\varepsilon_u/\pi$	Courant-Snyder invariant; emittance/ $\pi$ ( $u : x, y, l$ )
$\epsilon_R$	strength of a depolarizing resonance
$\eta$	phase slip factor, $\eta = \frac{1}{\gamma^2} - \alpha$
$\mu_u$	betatron phase advance per period, $\mu_u = \int_{\text{period}} \frac{ds}{\beta_u(s)}$ ( $u : x, y$ )
$\nu_u$	wave numbers, horizontal, vertical, synchrotron ( $u : x, y, l$ )
$\rho; \rho_0$	curvature radius; reference
$\sigma$	beam matrix
$\phi; \phi_s$	particle phase at voltage gap; synchronous phase
$\varphi_u$	betatron phase advance, $\varphi_u = \int ds/\beta_u$ ( $u : x, y, Y, \text{or } Z$ )
$\varphi$	spin angle to the vertical axis
$\omega_c$	critical angular frequency of SR, $\omega_c = 3\gamma^3 c/2\rho$
$\omega_s; \Omega_s$	$2\pi f_{\text{rev}}$ ; synchrotron frequency

5986 **9.1 Introduction**

5987 In the very manner that the 1930s-1940s cyclotron, betatron, microtron, weak fo-  
 5988 cusing synchrotron, which are still in use today, have since essentially not changed  
 5989 in their concepts and design principles, today the gap profile, yoke and current coil  
 5990 geometry of combined function alternating-gradient (AG) dipoles remain essentially  
 5991 as patented in 1950 (Fig. 9.1) [1].

**Fig. 9.1** Bending magnet pole profiles for a *focusing system for ions and electrons* [1]. Assuming curvature center to the left, the left (respectively right) profile is defocusing (resp. focusing), the middle profile has zero index

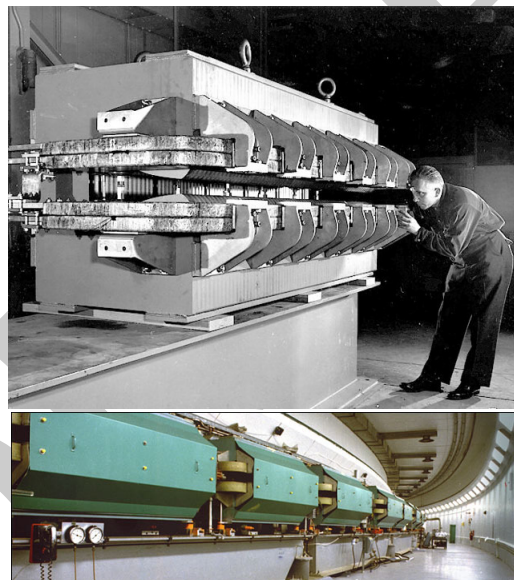
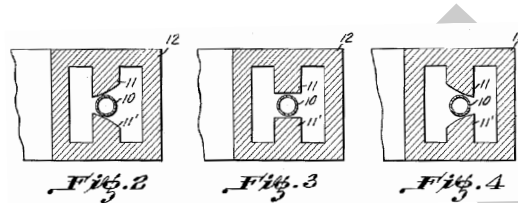


**Fig. 9.2** Top: the AGS combined function main dipole. The hyperbolic profile poles are visible, partly hidden by the field coils. Bottom: the 809 m circumference AGS synchrotron, comprised of 240 such dipoles [2]

5992 In 1952, in the context of studies concerning the Cosmotron, strong focusing  
 5993 was devised at the Brookhaven National Laboratory (BNL): “*Strong focusing forces*  
 5994 *result from the alternation of large positive and negative n-values in successive*  
 5995 *sectors of the magnetic guide field in a synchrotron. This sequence of alternately*

5996 *converging and diverging magnetic lenses [...] leads to significant reductions in*  
 5997 *oscillation amplitude” [3]. It led to the construction of the first two high-energy AG*  
 5998 *proton synchrotrons (PS), in the 30 GeV range, in the late 1950s: the CERN PS, and*  
 5999 *the AGS at BNL (Fig. 9.2). Both remain major pieces, 60 years later, of the respective*  
 6000 *injection chains of the two largest colliders in operation, the LHC and RHIC. Early*  
 6001 *works at BNL provided theoretical formalism, still at work today, for the analysis of*  
 6002 *beam dynamics in synchrotrons [4].*

**Fig. 9.3** SATURNE 2 strong focusing 3 GeV synchrotron at Saclay [5], successor in the late 1970s of SATURNE 1 weak focusing synchrotron (Fig. 8.1). It was the first strong focusing synchrotron to accelerate polarized ion beams



**Fig. 9.4** A quadrupole magnet at LBL in 1957, used for beam lines at the 184-inch cyclotron. An early specimen here, obviously, being a spin-off of the early 1950s concept of strong focusing [6]



6003 Separated function focusing, whereby beam guiding is ensured by uniform field  
 6004 dipoles while focusing is ensured separately by quadrupoles (Fig. 9.3), followed from  
 6005 the development of the latter (Fig.9.4), a spin-off of the strong index technology [7].

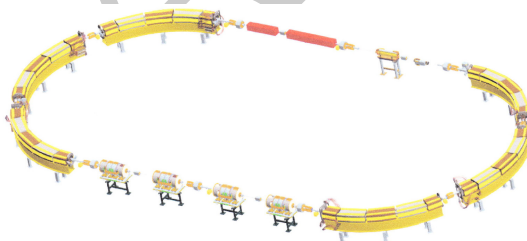
6006 The dramatic reduction of transverse beam size by strong focusing allows guid-  
 6007 ing and focusing magnets with small aperture, from lowest energies: medical syn-  
 6008 chrotrons in the 100 MeV range for instance, to highest ones: hundreds of GeV to  
 6009 multi-TeV range particle physics and nuclear physics colliders (Fig. 9.5). Beams in  
 6010 all these machines are essentially confined in a sub-centimeter or sub-millimeter  
 6011 scale transverse space. A synchrotron is a string of dipole and multipole magnets  
 6012 through which runs a vacuum pipe of a few centimeters diameter (hadron rings) or

6013 a few millimeters (electrons). The size of the ring is essentially determined by its  
 6014 circumference, proportional to the magnetic rigidity. This revolutionized the race to  
 6015 high energies, from the prior few GeV weak focusing synchrotrons and their huge  
 6016 magnets, to today's 7 TeV, 27 km long LHC and with further plans for 100 TeV, 100 km  
 6017 circumference colliders [8]. Strong focusing fostered the development of high en-  
 6018 ergy synchrotron light sources around the world, with high brightness synchrotron  
 6019 radiation (SR) from UV to gamma rays produced in electron storage rings in up to  
 6020 multi-GeV energy range.

**Fig. 9.5** In RHIC tunnel at the Brookhaven National Laboratory [2]. The two rings of the 255 GeV polarized proton beams and heavy ion collider run parallel over 3.8 km, and intersect at two experiments, STAR and SPHENIX



**Fig. 9.6** The ion rapid cycling medical synchrotron (iR-CMS) [9], an ion beam RCS for the treatment of cancer tumors



6021 AG focusing is still resorted to today, for instance in the hadrontherapy application  
 6022 (Fig. 9.6), light source lattice [10], and other high energy collider design [11], as  
 6023 it has the merit of compactness. On the other hand, the flexibility of separated  
 6024 function optics made it more popular: it allows to introduce modular functions in  
 6025 complex ring designs such as dispersion suppression sections, low-beta or insertion  
 6026 device sections, long straights, et cetera. Low-emittance, high-brightness light source  
 6027 lattices have complicated focusing further, by introducing longitudinal field gradient  
 6028 bending systems to minimize equilibrium beam emittance [12].

6029 Due to the necessary ramping of the field in order to maintain a constant orbit,  
 6030 synchrotron accelerators are pulsed, storage rings in some cases as well, high energy  
 6031 colliders in particular to bring beams to highest store energy. The acceleration is

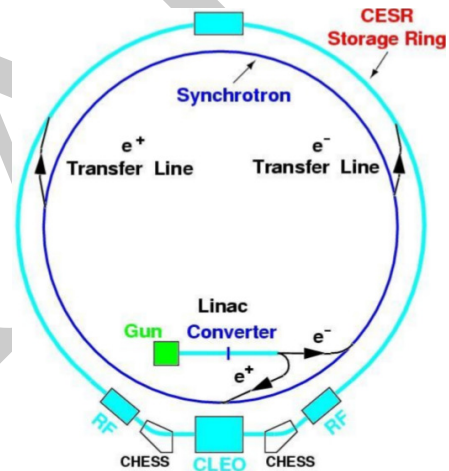
6032 cycled and the accelerating voltage frequency as well in ion accelerators, from  
 6033 injection to top energy. If the ramping uses a constant electromotive force, then  
 6034 (Eq. 8.3)

$$B(t) \approx \frac{t}{\tau} \quad (9.1)$$

6035  $\dot{B} = dB/dt$  does not exceed a few Tesla/second, thus the repetition rate of the  
 6036 acceleration cycle is of the order of a Hertz. If instead the magnet winding is part of  
 6037 a resonant circuit then the field oscillates,

$$B(t) = B_0 + \frac{\hat{B}}{2}(1 - \cos \omega t) \quad (9.2)$$

6038 so that, in the interval of half a voltage repetition period (*i.e.*,  $t : 0 \rightarrow \pi/\omega$ ) the  
 6039 field increases from an injection threshold value to a maximum value at highest  
 6040 rigidity,  $B(t) : B_0 \rightarrow B_0 + \hat{B}$ . The latter determines the highest achievable energy:  
 6041  $\hat{E} = pc/\beta = q\hat{B}\rho c/\beta$ . The repetition rate with resonant magnet cycling can reach a  
 6042 few tens of Hertz, a technique known as a rapid-cycling synchrotron (RCS). In both  
 6043 cases anyway  $B$  imposes its law and other parameters, comprising the acceleration  
 6044 cycle, the RF frequency in particular, will follow  $B(t)$ .



6045 **Fig. 9.7** Cornell rapid cycling  
 6046 synchrotron, 5 GeV injector of  
 6047 CESR storage ring [13]

6045 Instances of RCS rings include Cornell 12 GeV, 60 Hz electron AG synchrotron [14]  
 6046 (Fig. 9.7), commissioned in 1967 with a 7 GeV beam, a world record at the time, and  
 6047 still in operation half a century later as the injector of Cornell 5 GeV storage ring  
 6048 (CESR/CHES) [15]; Fermilab 8 GeV, 60 Hz Booster, which provides protons for  
 6049 the production of neutrino beams; the 30 GeV 500 kW proton beam J-PARC facility  
 6050 in Japan. Rapid cycling is also considered in ion-therapy applications (Fig. 9.6).

6051 To conclude on these preliminaries, let's mention the giants among accelerator  
 6052 facilities which nuclear (NP) and particle (HEP) physics research laboratories are:  
 6053 so far, strong focusing synchrotrons happen to be the building blocks from which

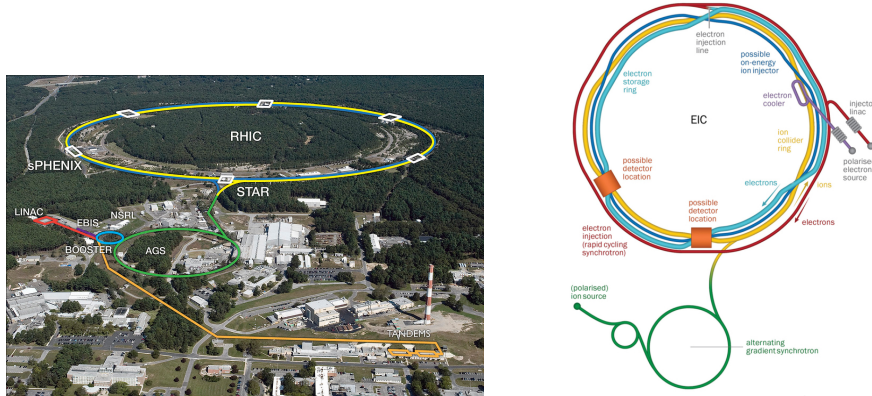


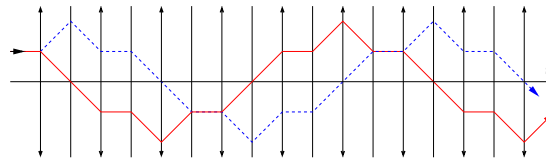
**Fig. 9.8** RHIC complex at the Brookhaven National Laboratory (left) [2], a cascade of 4 strong focusing ion synchrotrons: the AGS and its Booster, and the 3.8 km circumference intersecting RHIC rings, in motion towards the EIC project (right) [16] which will add 2 electron synchrotrons: an 18 GeV storage ring and its RCS injector

6054 they are constructed. This is so at the CERN LHC complex. This is apparent also in  
 6055 Fig. 9.8 which shows RHIC heavy ion collider complex, and its planned evolution,  
 6056 the Electron-Ion Collider [17]<sup>1</sup> The next colliders could be linacs, it was at SLAC  
 6057 with the SLC [18], it was the plan with such projects as TESLA [19], the NLC [20].  
 6058 The interest of NP and HEP will decide on the research tools: more large synchrotron  
 6059 rings for a muon collider [21], an FCC-ee, -hh and other -eh [8], or high gradient  
 6060 linacs for the ILC [22]. or for ReLic  $e^+e^-$  collider [23]. Or new acceleration methods  
 6061 and technologies?

6062 **9.2 Basic Concepts and Formulae**

Alternating gradient focusing is sketched in Fig. 9.9. An order of magnitude of

**Fig. 9.9** Horizontally focusing lenses (field index  $n \gg 0$ , the solid red trajectory) are vertically defocusing ( $n \ll 0$ , the dashed blue trajectory), and vice versa. This imposes alternating gradients in order for a sequence to be globally focusing, for both planes



<sup>1</sup> Beam polarization studies have been using zgoubi in all five EIC synchrotrons.

6063 the focusing index can be estimated from the fields met in these structures: say a  
 6064 maximum  $B \sim 1$  Tesla in the dipole gap, same at pole tip in quadrupoles  $\sim 10$  cm off  
 6065 axis. The latter results in  $\frac{\Delta B}{\Delta x} \sim 10$  T/m, the former in meters to tens of meters dipole  
 6066 curvature radius. All in all, in absolute value,  
 6067

$$n = -\frac{\rho}{B} \frac{\partial B}{\partial x} \sim \frac{10^{0-2}_{[m]}}{1_{[T]}} \times 10_{[T/m]} \sim 10^{1-3} \gg 1 \quad (9.3)$$

6068 much greater than in a weak focusing structure, characterized by  $0 < n < 1$ .

## 6069 9.2.1 Components of the Strong Focusing Optics

### 6070 Combined function (AG) optics

6071 This is, typically, the BNL AGS and CERN PS optics, using dipoles that ensure both  
 6072 beam guiding and focusing (Fig. 9.2). Separate quadrupole and multipole lenses have  
 6073 later been introduced as they provide knobs for the adjustment of optical functions  
 6074 and other parameters. AG optics is still topical in modern designs, as in the iRCMS  
 6075 whose six 60 deg arcs are comprised of a sequence of five focusing and defocusing  
 6076 combined function dipoles [9], Fig. 9.6.

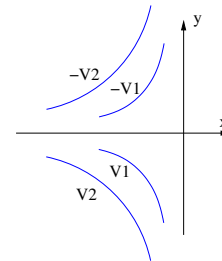
### 6077 Field

Referring to normal conducting magnet technology, a hyperbolic pole profile (Fig. 9.1) is an equipotential (a line of constant scalar potential  $V$ ) of equation

$$V_{\text{pole}} = Axy$$

at the origin of a magnetic field  $\mathbf{B} = \mathbf{grad} V$ , everywhere perpendicular to the equipotential. A combined function dipole with mid-plane geometrical symmetry is defined by materializing two equipotentials, at  $\pm V_{\text{pole}}$  (Fig. 9.10). This results in a

**Fig. 9.10** Symmetric materialization of pole profiles, at  $\pm V$ . Nothing would preclude materializing poles at  $V_1$  and  $-V_2$  potentials, with the same resulting field between the poles



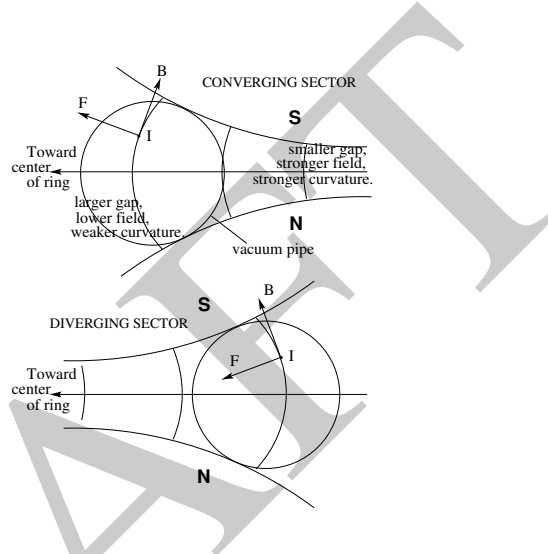


vertical field component  $B_y = \partial V / \partial y = Ax$ , and therefore a radial field index

$$n = -\frac{\rho}{B_y} \frac{\partial B_y}{\partial x} \Big|_{y=0} = \frac{\rho}{B_y} A$$

6078  $A$  is a constant, typically up to  $\sim 10$  T/m, *cf.* Eq. 9.3. The pole profile opens up towards  
 6079 either inward (toward the center of curvature, a horizontally focusing dipole, verti-  
 6080 cally defocusing) or outward (a vertically focusing dipole, horizontally defocusing),  
 Fig. 9.11.

**Fig. 9.11** Beam focusing in combined function dipoles. The center of curvature is to the left. The pole profile follows an equipotential  $V = Axy$ . Top: the pole profile opens up towards the center of curvature  $\rightarrow$  the dipole is horizontally converging (vertically diverging: current  $I$  comes out of the page, force  $F$  results from field  $B$ ). Bottom: pole profile closing toward the center of curvature  $\rightarrow$  the dipole is horizontally diverging, vertically converging



6081 In a bent AG dipole a line of constant field is an arc of a circle; the field guides  
 6082 the reference particle along the arc in the median plane. The mid-plane field can be  
 6083 expressed under the form  
 6084

$$B_y(r, \theta) = \mathcal{G}(r, \theta) B_0 \left( 1 + n \frac{r - r_0}{r_0} + n' \left( \frac{r - r_0}{r_0} \right)^2 + n'' \left( \frac{r - r_0}{r_0} \right)^3 + \dots \right) \quad (9.4)$$

6085 with  $r_0$  the reference (normally the orbit) radius. Higher order indices, sextupole  $n'$ ,  
 6086 octupole  $n''$ , ..., may be residual effects from fabrication tolerances, magnetic satu-  
 6087 ration, deformation of yoke with years, etc., or included by design, with significant  
 6088 value.

6089 In a straight AG dipole, a line of constant field is a straight line; an instance  
 6090 is the AGS main magnet (Fig. 9.2). Another instance is the Fermilab recycler arcs  
 6091 permanent magnet dipole, which includes quadrupole and sextupole components [24,  
 6092 25]. The modeling of the field in a straight combined function dipole can be derived  
 6093 from the scalar potential of Eq. 9.5.

### 6094 Separated function optics

6095 In a separated function lattice quadrupole lenses ensure the essential of the focusing,  
 6096 main bends have zero index. In smaller rings though, geometrical focusing in bending  
 6097 magnets may be significant (Sect. 8.2.1.2, Fig. 8.6). Wedge angles in addition may  
 6098 be introduced and contribute horizontal and vertical focusing/defocusing (Fig. 8.8).

6099 Higher order multipole lenses are used for the compensation of adverse effects:  
 6100 coupling, aberrations, space charge, impedance, etc., and for beam manipulations:  
 6101 controlling the coupling, resonant extraction, etc.

6102 The field in a multipole of order  $n$  ( $n = 1, 2, 3$ , etc.: dipole, quadrupole, sextupole,  
 6103 etc.) derives, via  $\mathbf{B} = \mathbf{grad}V$ , from the Laplace potential [26]

$$V_n = (n!)^2 \left\{ \sum_{q=0}^{\infty} (-)^q \alpha_{n,0}^{(2q)}(s) \frac{(x^2 + y^2)^q}{4^q q!(n+q)!} \right\} \left\{ \frac{x^{n-m} y^m}{m!(n-m)!} \sin m \frac{\pi}{2} \right\} \quad (9.5)$$

6104 where  $\alpha_{n,0}^{(2q)}(s) = d^{2q} \alpha_{n,0}(s) / ds^{2q}$  accounts for the  $s$ -dependence of the potential.  
 6105 Technologies for multipoles and combined multipoles include pole profiling, per-  
 6106 manent magnets [24, 27], superconducting  $\cos n\theta$  winding as in RHIC and LHC  
 6107 colliders, and variants.

6108 In a hard-edge field model the  $\sum_{q=0}^{\infty}$  series is reduced to the  $q = 0$  term, with the  
 6109 following outcomes [28, 29].

### 6110 Quadrupole

The equipotential (the pole profile) is an equilateral hyperbola, of equation  $Gxy = \text{constant}$  in an upright quadrupole (left figure below), and  $G(x^2 - y^2) = \text{constant}$  in a  $\pi/4$  skew quadrupole (right). The resulting field writes

$$B_x = \frac{\partial V}{\partial x} = Gy$$

$$B_y = \frac{\partial V}{\partial y} = Gx$$

$$B_x = Gx$$

$$B_y = -Gy$$

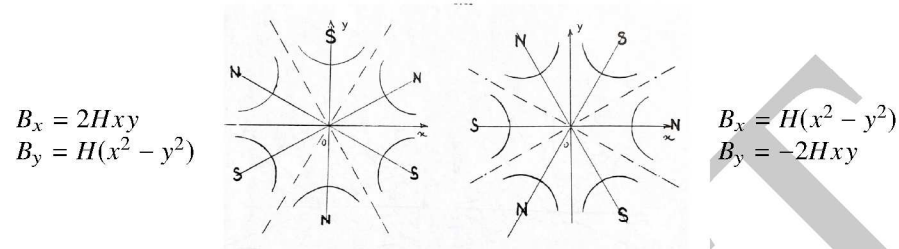
6111 Upright quadrupoles are used for focusing, skew quadrupoles are used to compensate,  
 6112 or introduce, transverse coupling. The focusing strength

$$K = \frac{1}{L} \frac{\int G(s) ds}{p/q} \quad (9.6)$$

6113 is momentum-dependent.

6114 *Sextupole*

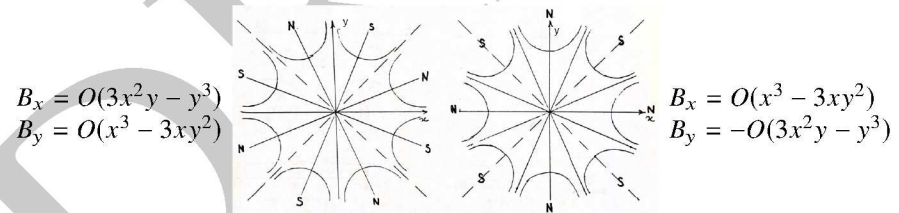
The equipotential satisfies  $H(3x^2y - y^3) = \text{constant}$  in an upright sextupole (left),  $H(x^3 - 3xy^2) = \text{constant}$  in a  $\pi/6$  skew sextupole (right), with resulting field



6115 Upright sextupoles introduce a vertical field component  $B_y \propto x^2$ , they are used  
 6116 to correct optical aberrations, to modify the momentum dependence of the wave  
 6117 numbers  $\nu_x, \nu_y$ , and in beam manipulations such as resonant extraction. Skew  
 6118 sextupoles introduce a radial field component  $B_x \propto y^2$ , they are used to correct  
 6119 optical aberrations.

6120 *Octupole*

The equipotential pole profile satisfies  $O(x^3y - xy^3) = \text{constant}$  in an upright octupole (left),  $O(x^4 - 6x^2y^2 + y^4) = \text{constant}$  in a  $\pi/8$  skew octupole (right), yielding the field



6121 Upright octupoles are used to introduce a vertical field component  $B_y \propto x^3$ ; skew  
 6122 octupoles introduce a vertical field component  $B_y \propto y^3$ . Octupoles are used to correct  
 6123 aberrations, or to modify the amplitude dependence of wave numbers.

## 6124 9.2.2 Transverse Motion

6125 The transverse motion of a particle in the  $S$ -periodic lattice of a cyclic accelerator,  
6126 at design momentum  $p_0$  and with curvature radius  $\rho_0$ , satisfies Hill's equations<sup>2</sup>

$$\frac{d^2x}{ds^2} + K_x(s)x = \frac{1}{\rho_0} \frac{\Delta p}{p_0}, \quad \frac{d^2y}{ds^2} + K_y(s)y = 0 \quad (9.7)$$

6127 where  $K_x(s)$ ,  $K_y(s)$  have the periodicity of the lattice ( $K_x(s+S) = K_x(s)$ ), and  
6128 depend locally on the nature of the optical elements, in the following way.

6129 Case of

$$\text{-- dipole : } \begin{cases} K_x = \frac{1-n}{\rho_0^2} \\ K_y = \frac{n}{\rho_0^2} \end{cases} \quad \left( n = -\frac{\rho_0}{B_0} \frac{\partial B_y}{\partial x} \right) \quad (9.8)$$

6130

$$\text{-- a wedge at } s = s_w : \begin{cases} K_x \\ K_y \end{cases} = \pm \frac{\tan \varepsilon}{\rho_0} \delta(s - s_w) \quad \left( \text{with } \varepsilon \lesseqgtr 0 \text{ if } \begin{matrix} \text{focusing} \\ \text{defocusing} \end{matrix} \right)$$

6131

$$\text{-- quadrupole : } K_x = \frac{\pm G}{B\rho}; \quad \frac{1}{\rho_0} = 0 \quad \left( \text{gradient } G = \frac{\text{field at pole tip}}{\text{radius at pole tip}} \right)$$

6132

$$\text{-- drift space : } K_x = K_y = 0; \quad \frac{1}{\rho_0} = 0$$

6133 By contrast with the betatron and weak focusing technologies, strong focusing  
6134 with its independent focusing ( $G > 0$ ) and defocusing ( $G < 0$ ) gradient families  
6135 allows separate adjustment of the horizontal and vertical focusing strengths, and  
6136 wave numbers as a consequence.

6137 The on-momentum ( $p = p_0$ ) closed orbit coincides with the reference axis of  
6138 the optical elements. The betatron motion for an on-momentum particle satisfies  
6139 Eq. 9.7 with  $\Delta p = 0$ . Solving the latter (see Sect. 8.2.1.3) requires introducing two  
6140 independent solutions  $u_1(s)$  (Eq. 8.12), the linear combination of which yields the  
6141 pseudo harmonic motion (Eq. 8.14)

$$\begin{cases} u(s) = \sqrt{\beta_u(s)\varepsilon_u/\pi} \cos\left(\int \frac{ds}{\beta_u(s)} + \varphi_u\right) \\ u'(s) = -\sqrt{\frac{\varepsilon_u/\pi}{\beta_u(s)}} \sin\left(\int \frac{ds}{\beta_u(s)} + \varphi_u\right) + \alpha(s) \cos\left(\int \frac{ds}{\beta_u(s)} + \varphi_u\right) \end{cases} \quad (9.9)$$

6142 The motion satisfies the Courant-Snyder invariant, namely (Fig. 9.12)

<sup>2</sup> Acceleration, or deceleration, adds a velocity term, betatron damping results. This is addressed in "Betatron damping", Sect. 10.2.3, where it accounts in addition for a non-constant varying orbital radius.

$$\gamma_u(s)u^2 + 2\alpha_u(s)uu' + \beta_u(s)u'^2 = \frac{\epsilon_u}{\pi} \tag{9.10}$$

6143 *i.e.*, the surface of the phase space ellipse is a constant of the motion. Its form  
 6144 and orientation (Fig. 9.12) change along the period as a consequence of the strong  
 6145 modulation of the betatron functions (Fig. 9.13), far more than in a weak focusing  
 6146 lattice which features weak betatron modulation:  $\alpha_u(s) \approx 0$  and  $\beta_u(s) \approx \text{constant}$   
 6147 (Figs. 8.9, 8.10).

**Fig. 9.12** Courant-Snyder invariant and turn-by-turn harmonic motion along the invariant, observed at some azimuth  $s$ . The aspect ratio of the ellipse depends on the observation azimuth  $s$  but its area  $\epsilon_u$  is invariant

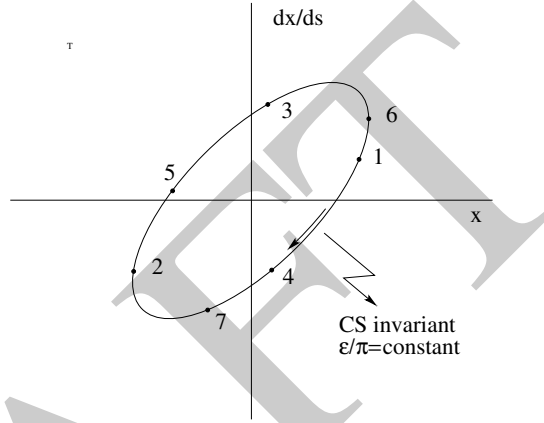
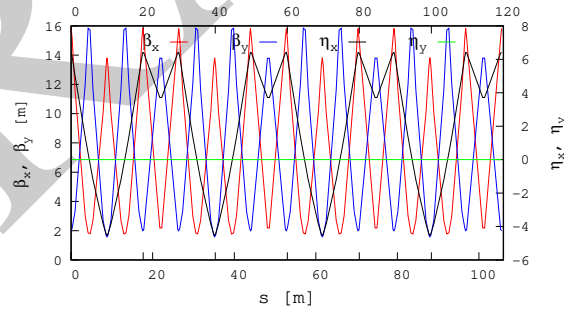


**Fig. 9.13** Optical functions around SATURNE2 synchrotron, a 4-period FODO cell lattice



6148 Beam envelopes are given by the extrema,

$$\hat{x}_{\text{env}}(s) = \pm \sqrt{\beta_x(s) \frac{\epsilon_x}{\pi}}, \quad \hat{y}_{\text{env}}(s) = \pm \sqrt{\beta_y(s) \frac{\epsilon_y}{\pi}} \tag{9.11}$$

6149 *Phase space motion*6150 Write the two independent solutions  $u_{1,2}(s)$  (Eq. 8.12) under the form

$$u_1(s) = \underbrace{F(s)}_{S\text{-periodic}} \times \underbrace{e^{i\mu\frac{s}{S}}}_{\frac{2\pi S}{\mu}\text{-periodic}} \quad \text{and} \quad u_2(s) = u_1^*(s) = F^*(s) e^{-i\mu\frac{s}{S}} \quad (9.12)$$

6151 where

$$F(s) = \sqrt{\beta_u(s)} e^{i\left(\int_0^s \frac{ds}{\beta_u(s)} - \mu\frac{s}{S}\right)} \quad (9.13)$$

6152 Introduce

$$\psi_u(s) = \int_0^s \frac{ds}{\beta_u(s)} - \mu\frac{s}{S} \quad (9.14)$$

6153 so that  $F(s) = \sqrt{\beta_u(s)} e^{i\psi_u(s)}$ . Equation 9.9 thus takes the form

$$\begin{cases} u(s) = \underbrace{\sqrt{\beta_u(s)}\varepsilon_u/\pi}_{S\text{-periodic}} \underbrace{\cos\left[\nu\frac{s}{R} + \underbrace{\psi_u(s)}_{S\text{-per.}} + \varphi_u\right]}_{\frac{2\pi S}{\mu}\text{-periodic}} \\ u'(s) = -\sqrt{\frac{\varepsilon_u/\pi}{\beta_u(s)}} \sin\left[\nu\frac{s}{R} + \psi_u(s) + \varphi_u\right] + \alpha(s) \cos\left[\nu\frac{s}{R} + \psi_u(s) + \varphi_u\right] \end{cases} \quad (9.15)$$

6154 where  $\nu = \frac{N\mu}{2\pi}$ . Thus, as the betatron function  $\beta_u(s)$  and phase  $\psi_u(s)$  are  $S$ -periodic,  
 6155 the turn-by-turn motion observed at a given azimuth  $s$  (*i.e.*,  $u(s)$ ,  $u(s+S)$ ,  $u(s+2S)$ ,  
 6156 ...) is sinusoidal and its frequency is  $\nu = N\mu/2\pi$ . Successive particle positions  
 6157 ( $u(s)$ ,  $u'(s)$ ) in phase space lie on the Courant-Snyder invariant (Eq. 9.10). The  
 6158 working point  $(\nu_x, \nu_y)$  fully characterizes the first order optical setting of the lattice.

6159 *Off-momentum motion*

6160 The motion of an off-momentum particle satisfies the inhomogeneous Hill's hori-  
 6161 zontal differential Eq. 9.7. The chromatic closed orbit

$$x_{\text{ch}}(s) = D_x(s) \frac{\delta p}{p} \quad (9.16)$$

6162 is a particular solution of the equation, its periodicity is that of the cell.

6163 By contrast with a weak focusing lattice where chromatic closed orbits are parallel  
 6164 (Eq. 8.26), in a strong focusing lattice they are distorted (Fig. 9.13), their excursion  
 6165 depends on the distribution along the cell of (i) the dispersive elements which are  
 6166 the dipoles, and (ii) the focusing.

6167 The horizontal motion of an off-momentum particle is a superposition of the par-  
 6168 ticular solution (Eq. 9.16) and of the betatron motion, solution of the homogeneous  
 6169 Hill's equation (Eq. 9.15), namely

$$x(s) = x_\beta(s) + x_{\text{ch}}(s) = \sqrt{\beta_x(s) \frac{\varepsilon_x}{\pi}} \cos \left( \int \frac{ds}{\beta_x} + \varphi_x \right) + D_x(s) \frac{\delta p}{p_0} \quad (9.17)$$

6170 whereas the vertical motion is unchanged (Eq. 9.15 taken for  $u(s) \equiv y(s)$ ).

### 6171 Chromaticity

6172 The focusing strength of combined function dipoles and quadrupoles is a decreasing  
 6173 function of particle rigidity  $B\rho = p/q$  (Eq. 9.8). In a ring this affects the horizontal  
 6174 and vertical wave numbers, an effect quantified as the chromaticity,  $\xi_{x,y}$ . To the first  
 6175 order in  $\delta p/p$ , this writes

$$\delta \nu_{x,y} = \xi_{x,y} \frac{\delta p}{p} \quad (9.18)$$

6176 A linear lattice has a natural chromaticity. Over a distance  $\mathcal{L}$  it is given by

$$\xi_{x,y} = \frac{-1}{4\pi} \int_{\mathcal{L}} \beta_{x,y}(s) K_{x,y}(s) ds \quad (9.19)$$

6177 Use a circular integral,  $\oint$  in the case of a ring. The natural chromaticity is a negative  
 6178 quantity: focusing decreases with increasing momentum.

6179 One consequence of the chromaticity is that beam momentum spread  $\delta p/p$  results  
 6180 in a tune spread  $\delta \nu_{x,y} = \xi_{x,y} \times \delta p/p$ , a beam occupies an extended area in the tune  
 6181 diagram. For this reason in particular, the chromaticity is usually corrected. This is  
 6182 realized by placing sextupoles in dispersive sections, at least two families: a family  
 6183 of horizontal lenses (strength  $H_x$ ) located at large  $\beta_x$  and a family of vertical lenses  
 6184 (strength  $H_y$ ) located at large  $\beta_y$ .

6185 The effect leaned on is the following:

6186 - betatron motion  $x_\beta(s)$  of particles with momentum  $p_0 + \Delta p$  is around an off-  
 6187 centered, chromatic closed orbit  $x_{\text{ch}}(s)$  (Eq. 9.16);

6188 - introducing a sextupole results in a local gradient as  $B_y \propto (x_{\text{ch}} + x_\beta)^2 =$   
 6189  $x_{\text{ch}}^2 + 2x_{\text{ch}}x_\beta + x_\beta^2$ , namely,  $\left. \frac{\partial B_y}{\partial x} \right|_{x=x_{\text{ch}}} = 2x_{\text{ch}} = 2D_x \frac{\Delta p}{p}$ . This results in a focusing force

6190 proportional to  $\delta p/p$ . Sextupoles contribute to chromaticity (or its compensation)  
 6191 following

$$\xi_{x,y} = \frac{1}{4\pi} \int H_{x,y}(s) \beta_{x,y}(s) D_x(s) ds \quad (9.20)$$

### 6192 9.2.3 Resonances

6193 Consider the excitation of transverse beam motion by a generator of frequency  $\Omega$   
 6194 located at some azimuth along the ring [29]. The action of the excitation  $S \times \sin \Omega t$   
 6195 on the oscillating motion  $u(t)$  can be written under the form

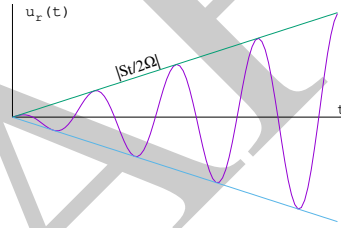
$$\frac{d^2 u}{dt^2} + \omega^2 u = S \sin \Omega t \quad (9.21)$$

6196 Assume harmonic motion for simplicity (as in a weak focusing lattice). Take gen-  
 6197 erator amplitude  $S = \text{constant}$ , the solution (superposition of the solution of the ho-  
 6198 mogeneous differential equation and of a particular solution of the inhomogeneous  
 6199 differential equation) writes

$$u(t) = U \cos(\omega t + \varphi_u) + \frac{S}{\omega^2 - \Omega^2} \sin \Omega t \quad (9.22)$$

If betatron motion and excitation are in synchronism, *i.e.* on the resonance,  $\omega = \Omega$ ,  
 a particular solution of Eq. 9.21 is

$$u_r(t) = -\frac{St}{2\Omega} \cos \Omega t$$



6200 the amplitude of the oscillatory motion grows rapidly with time, at a rate  $|St/2\Omega|$ .

Assume the amplitude  $S$  to be  $T'$ -periodic instead, angular frequency  $\omega' = 2\pi/T'$ ,  
 take its Fourier expansion

$$S(t) = \sum_{p=0}^{\infty} a_p \cos(p\omega' t + \varphi_p)$$

6201 the equation of motion thus writes

$$\frac{d^2 u}{dt^2} + \omega^2 u = \sum_{p=0}^{\infty} a_p \cos(p\omega' t + \varphi_p) \sin \Omega t = \sum_{p=0}^{\infty} \frac{a_p}{2} \left[ \sin[(\Omega - p\omega')t + \varphi_p] + \sin[(\Omega + p\omega')t + \varphi_p] \right] \quad (9.23)$$

6202 Resonance may occur at generator frequencies  $\Omega = \omega \pm p\omega'$ , the strength depends  
 6203 on the amplitude  $a_p$  of the excitation harmonics. A generator at some point in the  
 6204 lattice excites all harmonics with equal amplitudes  $a_p$ . In the case of an extended  
 6205 excitation source, low harmonics only matter.



6206 *Sextupole and octupole resonances*6207 The horizontal motion in the presence of sextupoles ( $B_y(\theta)|_{y=0} = S(\theta)x^2$ ) satisfies

$$\frac{d^2x}{d\theta^2} + \nu_x^2 x = S(\theta)x^2 \quad (9.24)$$

6208 Assume weak perturbation of the motion, so that  $x(\theta) \approx \hat{x} \cos(\nu_x \theta + \varphi_x)$ , the solution  
 6209 for unperturbed motion. Assume also  $S(\theta)$   $2\pi$ -periodic. Substitute its Fourier series  
 6210 expansion  $S(\theta) = \sum_{p=0}^{\infty} a_p \cos(p\theta + \varphi_p)$  in Eq. 9.24, develop to get

$$\frac{d^2x}{d\theta^2} + \nu_x^2 x = \frac{\hat{x}^2}{2} \left[ \sum_{p=0}^{\infty} a_p \cos(p\theta + \varphi_p) + \frac{1}{2} \sum_{p=0}^{\infty} a_p \left[ \cos[(p - 2\nu_x)\theta + \varphi_p - 2\varphi_x] + \cos[(p + 2\nu_x)\theta + \varphi_p + 2\varphi_x] \right] \right] \quad (9.25)$$

Thus resonance may occur at the betatron frequency families  $\nu_x = \pm p$ ,  $\nu_x = \pm(p - 2\nu_x)$ , and  $\nu_x = \pm(p + 2\nu_x)$ , *i.e.*,

$$\begin{cases} \nu_x = p \\ 3\nu_x = p \end{cases}$$

6211 In the case of a single sextupole in the ring, all the harmonics  $p$  are excited with the  
 6212 same amplitude  $a_p$ .

An octupole introduces a field component  $B_y(\theta)|_{y=0} = O(\theta)x^3$ . A similar development yields

$$\begin{cases} \nu_x = p \\ 2\nu_x = p \\ 4\nu_x = p \end{cases}$$

Resonances in a general manner occur at betatron frequencies satisfying

$$m\nu_x + n\nu_y = \text{integer}$$

6213 In this coupling regime one has

$$\frac{\varepsilon_x}{m} - \frac{\varepsilon_y}{n} = \text{constant}, \quad \text{an invariant of the motion} \quad (9.26)$$

6214 From this it results that,

6215 - if  $m$  and  $n$  have opposite signs the resonance causes energy exchange between  
 6216 the horizontal and vertical motions:  $\frac{\varepsilon_x}{|m|} + \frac{\varepsilon_y}{|n|} = \text{constant}$ , an increase of  $\varepsilon_x$  correlates  
 6217 with a decrease of  $\varepsilon_y$  and vice-versa. In the presence of linear coupling for instance,  
 6218  $\nu_x - \nu_y = \text{integer}$ ,  $\varepsilon_x + \varepsilon_y = \text{constant}$ . An increase in motion amplitude anyway may  
 6219 cause particle loss, an issue in cyclotrons where the Walkinshaw resonance  $\nu_x = 2\nu_y$   
 6220 causes vertical beam loss due to the increase of  $\varepsilon_y$ ;

6221 - if  $m$  and  $n$  have the same sign the resonance is liable to induce motion instability:  
 6222  $\frac{\varepsilon_x}{m} - \frac{\varepsilon_y}{n} = \text{constant}$ ,  $\varepsilon_x$  and  $\varepsilon_y$  may both increase with no limit.

### 6223 Resonant Extraction

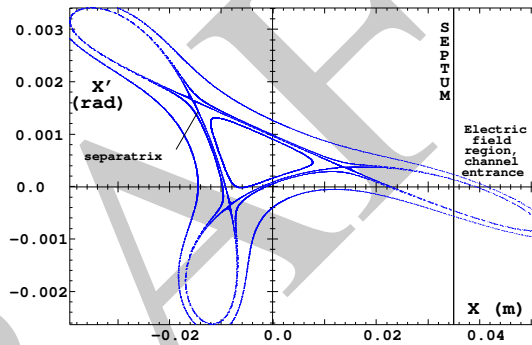
6224 Resonant extraction is based on the effect of a non-linear force on a dynamical  
 6225 system. A linear regime, under the effect of linear forces, satisfies Eq. 9.7. If  $x(s)$  is  
 6226 a stable solution, so is  $\lambda x(s)$  ( $\lambda$  a proportionality constant). Introducing a non-linear  
 6227 force modifies the equation of motion, into for instance

6228  $\diamond \frac{d^2x}{ds^2} + K_x(s)x = S(s)x^2$ : sextupole perturbation,

6229  $\diamond \frac{d^2x}{ds^2} + K_x(s)x = O(s)x^3$ : octupole perturbation,

6230 If  $x(s)$  is a stable solution, it may no longer be the case for  $\lambda x(s)$ . If  $x(s)$  is small  
 6231 enough the motion, subject to linear and non-linear forces, is quasi-linear and stable.  
 6232 However, increasing the motion amplitude will at some point result in unstable  
 6233 motion. In the  $(x, x')$  phase space, the stable regime is bounded by a separatrix.  
 Outside the latter the motion is essentially unstable, or liable to reach amplitudes

**Fig. 9.14** Horizontal motion near a 3rd integer resonance. Within the triangle separatrix the motion is stable. Outside the triangle, motion reaches large amplitudes. An electrostatic septum extracts particles which jump to the right of the septum (into the extraction channel) during their motion



6234 beyond transverse acceptance of the accelerator (Fig. 9.14).  
 6235

### 6236 9.2.4 Acceleration. Synchrotron Motion

6237 Particle motion in longitudinal phase space (phase, momentum) and its stability  
 6238 are determined by the lattice and by the acceleration parameters, as introduced in  
 6239 Sect. 8.2.2. They include the

- 6240 - RF  $f_{rf} = hf_{rev}$ ,
- 6241 - voltage  $V(t) = \hat{V} \sin \int \omega_{rf} dt$ ,
- 6242 - synchronous phase  $\phi_s$  (phase of the particle in synchronism with the RF oscillation), which increases by  $2\pi h$  per turn,
- 6243 - transition  $\gamma_{tr} = 1/\sqrt{\alpha}$  (Fig. 8.15).

In the case of weakly modulated betatron functions (weak focusing lattice; AG lattice to some extent),  $\alpha \approx 1/v_x^2$  so that

$$\gamma_{tr} \approx \nu_x$$

6244 This is the case of SATURNE 1: a weak focusing lattice (see Chap. 8 and simulation  
6245 exercises there) operated above transition as  $\gamma_{tr} = \nu_x \approx 0.6$ . In the AGS at BNL the  
6246 working point is  $\nu_x \approx 8.7$  whereas  $\gamma_{tr} = 8.4 \approx \nu_x$ ; transition is crossed as proton  
6247 beams are accelerated from  $\gamma \approx 3$  to  $\gamma \approx 25$ . Instead, SATURNE 2 strong focusing  
6248 lattice was operated at negative  $\alpha$ ,  $\eta = \frac{1}{\gamma^2} - \alpha$  does not cancel,  $\gamma_{tr}$  is pure imaginary.

The energy gain per turn at the cavity is

$$\Delta W = 2\pi R q \rho \dot{B} = q \hat{V} \sin \phi_s$$

$\Delta W$  is imposed by the field law in order to ensure that at all time the synchronous particle momentum satisfies

$$p_s(t) = qB(t)\rho$$

### 6249 Phase stability

6250 Particles with phase and momentum offsets  $(\Delta\phi, \Delta p/p_s) = (\phi - \phi_s, (p - p_s)/p_s)$   
6251 in the vicinity of the synchronous particle at  $(\phi_s, p_s)$  undergo periodic longitudinal oscillations. The longitudinal motion satisfies the differential equations

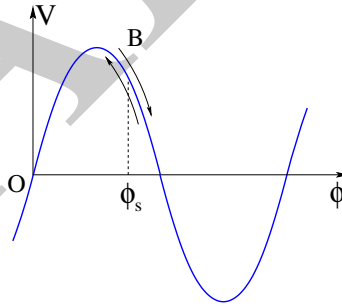


**Fig. 9.15** In the presence of RF, particles oscillate in the vicinity of the synchronous phase. Above transition, in this schematic

6252

$$\frac{d\Delta\phi}{dt} = h\eta\omega_s \frac{\Delta p}{p}, \quad \frac{d(\Delta p/p)}{dt} = \frac{e\hat{V}\omega_s}{2\pi\beta_s^2 E_s} [\sin \phi - \sin \phi_s] \quad (9.27)$$

6253 If peak amplitudes are small the differential Eqs. 9.27 yield

$$\frac{d^2\Delta\phi}{dt^2} + \Omega_s^2\Delta\phi = 0 \quad (9.28)$$

6254 the motion is sinusoidal, with a synchrotron angular frequency

$$\Omega_s = \frac{c}{R} \sqrt{\frac{|\eta| h q \hat{V} \cos \phi_s}{2\pi E_s}} \quad (9.29)$$

6255 The synchrotron tune, number of synchrotron oscillations per revolution, writes

$$\nu_s = \frac{\Omega_s}{\omega_{\text{rev}}} = \frac{1}{\beta_s} \sqrt{\frac{\eta h q \hat{V} \cos \phi_s}{2\pi E_s}} \quad (9.30)$$

Synchrotron oscillations are slow compared to betatron oscillations, typically  $\nu_s \sim \nu_{x,y}/10^{2\sim 3}$ . Motion stability requires  $\Omega_s^2 > 0$ , or

$$\eta \cos \phi_s > 0$$

6256 Longitudinal motion in  $(\phi, \dot{\phi}/\Omega_s)$  phase space is on a circle. The extent in phase and  
6257 energy, or momentum, of the small amplitude oscillations satisfy

$$\widehat{\Delta\phi} = \frac{h\eta E_s}{p_s R \Omega_s} \frac{\widehat{\Delta E}}{E_s} = \frac{h\eta E_s}{p_s R \Omega_s} \beta_s^2 \frac{\widehat{\Delta p}}{p} \quad (9.31)$$

6258 The bunch length is

$$L_{\text{bunch}} = \frac{R}{h} \widehat{\Delta\phi} \quad (9.32)$$

6259 *Separatrix*

6260 If peak amplitudes are large the oscillations are non-linear and, assuming slow  
6261 acceleration, by combining Eqs. 9.27,

$$\frac{d^2 \Delta\phi}{dt^2} + \Omega_s^2 \frac{\sin \phi - \sin \phi_s}{\cos \phi_s} = 0 \quad (9.33)$$

6262 A first integral of this equation is the equation of the separatrix (Fig. 9.16)

$$\frac{\dot{\phi}}{2} - \Omega_s^2 \frac{\cos \phi + \phi \sin \phi_s}{\cos \phi_s} = -\Omega_s^2 \frac{\cos(\pi - \phi_s) + (\pi - \phi_s) \sin \phi_s}{\cos \phi_s} \quad (9.34)$$

6263 This defines two locations where  $\dot{\phi}$  changes sign, *i.e.*  $\dot{\phi} = 0$ , namely,

6264 (i)  $\phi_1 = \pi - \phi_s$ ,

6265 (ii)  $\phi_2$  such that  $\cos \phi_2 + \phi_2 \sin \phi_s = \cos(\pi - \phi_s) + (\pi - \phi_s) \sin \phi_s$ .

6266 The motion is stable, oscillatory, within the domain  $\phi \in [\phi_1, \phi_2]$ , the “bucket”, and  
6267 unbounded beyond. The bucket height is obtained for  $\phi = \phi_s$ , namely, from Eq. 9.34

$$\frac{\dot{\phi}_{\text{max}}}{\Omega_s} = \sqrt{2[2 - (\pi - 2\phi_s) \tan \phi_s]} \quad (9.35)$$

6268 Expressed in momentum,

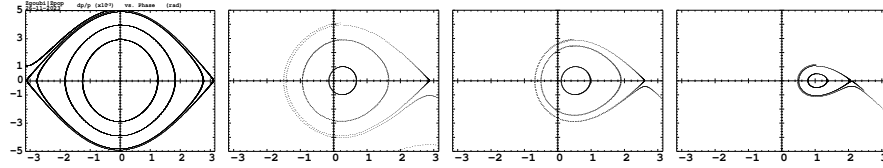
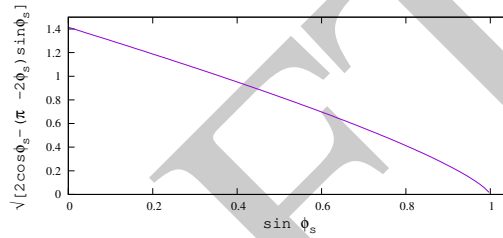


**Fig. 9.16** Longitudinal motion separatrix in  $(\phi, dp/p)$  phase space, and some stable as well as unbounded motions. Case of SATURNE 2 at injection energy, 50 MeV. From left to right: case of  $\phi_s = 0$  (stationary bucket),  $\phi_s = 15, 30$ , and  $60$  deg. Small motions are centered on  $\phi_s$ , their synchrotron tunes satisfy Eq. 9.30. The momentum acceptance (height of the separatrix) satisfies Eq. 9.36, with respectively  $\pm \frac{\Delta p}{p} \approx 0.00496, 0.00392, 0.00290$  and  $0.00107$

**Fig. 9.17** Dependence of the momentum extent of the bucket (normalized to  $\frac{1}{\beta_s} \sqrt{\frac{q\hat{V}}{\pi h \eta E_s}}$ ) on the synchronous phase  $\phi_s$ . It takes its value in  $\sqrt{2} \rightarrow 0$  for  $\sin \phi_s : 0 \rightarrow 1$



$$\pm \frac{\Delta p}{p} = \pm \frac{1}{\beta_s} \sqrt{\frac{q\hat{V}}{\pi h \eta E_s} [2 \cos \phi_s - (\pi - 2\phi_s) \sin \phi_s]} \quad (9.36)$$

6269 Its dependence on  $\phi_s$  is represented in Fig. 9.17. Stationary bucket mode, *i.e.*  $\sin \phi_s =$   
 6270  $0$ , has greatest acceptance. The latter decreases in accelerated bucket mode as  $\phi_s \rightarrow$   
 6271  $\pi/2$  (Fig. 9.16).

#### 6272 *Adiabatic damping of synchrotron oscillations*

6273 The equation of motion, Eq. 9.33, assumes a slow acceleration rate,  $dT_{\text{rev}}/dt \ll 1$ ,  
 6274 such that  $p_s(t)$ ,  $\eta$ , possibly  $\hat{V}$ , and thus  $\Omega_s$  change slowly during synchrotron oscillations  
 6275 and therefore can be considered constant. The extreme phase and momentum  
 6276 excursions during acceleration satisfy

$$\begin{aligned} \widehat{\Delta\phi} &\propto \left( \frac{\eta}{R^2 \gamma \hat{V} \cos \phi_s} \right)^{1/4} \\ \frac{\widehat{\Delta p}}{p} &\propto \frac{1}{\beta_s} \left( \frac{\hat{V} \cos \phi_s}{\eta \gamma^3 R^2} \right)^{1/4} \end{aligned} \quad (9.37)$$

6277 In the case of acceleration on a fixed orbit (constant radius  $R$ ),

$$\widehat{\Delta\phi} \times \widehat{\Delta p} = \text{constant} \quad (9.38)$$

6278 *Adiabatic damping of the betatron oscillations*

6279 The mechanism is described in Sect. 8.2.2 (Fig. 8.14), the equations of motion  
6280 are addressed in Sect. 10.2.3. In the case of an adiabatic change of momentum  
6281  $p = \beta\gamma m_0 c$  (a slow change compared to the betatron motion oscillation frequency)  
6282 the transverse motion damping satisfies

$$p \varepsilon_u = \text{constant}, \quad \text{or} \quad \beta\gamma\varepsilon_u = \text{constant} \quad (9.39)$$

6283 Coordinate damping satisfies (Eq. 10.22 with orbit radius  $R = \text{constant}$ )

$$x, y \propto 1/\sqrt{p}, \quad x', y' \propto 1/\sqrt{p} \quad (9.40)$$

## 6284 9.2.5 Synchrotron Radiation, Dynamical Effects

6285 Emittance growth upon SR matters in high  $\gamma$  rings, electron rings so far, muon  
6286 collider possibly in the future [30] and other FCC lepton and hadron collider [8].

6287 The stochastic nature of SR and the energy loss it results in, have been introduced  
6288 in Chap. 5. Dynamical effects in a synchrotron ring are further addressed here [31,  
6289 32].

6290 *Motion invariants*

6291 In the absence of perturbation by synchrotron radiation, particle motion satisfies the  
6292 Courant-Snyder (Eq. 9.41) and longitudinal (Eq. 9.42) phase-space invariants

$$\varepsilon_u = \gamma_u(s)u^2 + 2\alpha_u(s)uu' + \beta_u(s)u'^2 \quad (u = x \text{ or } y) \quad (9.41)$$

6293

$$\varepsilon_l = \frac{\alpha E_s}{2\Omega_s} \left( \frac{\delta E}{E_s} \right)^2 \quad (9.42)$$

6294 Under the effect of stochastic SR, individual invariants can in general not be de-  
6295 termined, averages over particle ensembles are considered instead (noted  $\overline{(\ast)}$  in the  
6296 following), they evolve according to

$$\frac{d\overline{\varepsilon}_u}{dt} = -\frac{\overline{\varepsilon}_u}{\tau_u} + C_u \quad (9.43)$$

6297 towards a stationary solution

$$\varepsilon_{n,eq} = C_u \tau_u \quad (9.44)$$

6298 where  $C_u$  is a constant at fixed energy (storage ring), with characteristic time

$$\tau_u = \frac{T_{rev} E_s}{U_s J_u} \tag{9.45}$$

6299  $J_{n=x,y,l}$  are the partition numbers (lattice properties), respectively horizontal, vertical,  
6300 longitudinal,

$$J_x = 1 - \mathcal{D}, \quad J_y = 1, \quad J_l = 2 + \mathcal{D} \tag{9.46}$$

where

$$\mathcal{D} = \frac{\overline{D_x(1 - 2n)}/\rho^3}{1/\rho^2}$$

6301 In this expression,  $\overline{(*)} = \frac{1}{2\pi R} \int_{\text{dipoles}} (*) ds$ ,  $n$  is the field index - case of combined  
6302 function dipoles,  $D_x$  is the dispersion function, The partition numbers satisfy the  
6303 Robinson theorem

$$J_x + J_y + J_l = 4 \tag{9.47}$$

**Table 9.1** Common expressions for the energy loss per turn,  $U_s$  (E-loss), for the damping times and equilibrium emittances, in the hypothesis of an isomagnetic lattice. Their scaling with  $\gamma$  is given in the 2nd row

	E-loss	$\epsilon_{l,eq}$	$\sigma_l$	$\tau_l$	$\epsilon_{x,eq}^1$	$\tau_x$	$\epsilon_{y,eq}$	$\tau_y$
Scaling :	$\gamma^4$	$\gamma^{3/2}$	$1/\gamma^{1/2}$	$1/\gamma^3$	$\gamma^2$	$1/\gamma^3$		$1/\gamma^3$
	$C_\gamma \frac{E_s^4}{\rho}$	$\frac{\alpha E_s}{\Omega_s} \frac{C_q \gamma^2}{J_l \rho}$	$\frac{\alpha c}{\Omega_s} \sigma_{\frac{\Delta E}{E}}$	$\frac{T_{rev} E_s}{U_s J_l}$	$\frac{C_q \gamma^2 \overline{\mathcal{H}}}{J_x \rho}$	$\frac{T_{rev} E_s}{U_s J_x}$	$\ll \epsilon_x$	$\frac{T_{rev} E_s}{U_s J_y}$

[1]  $\overline{\mathcal{H}} = \frac{1}{L_{dip}} \int_{dip} \frac{ds}{\beta_x} [D_x^2 + (\alpha_x D_x + \beta_x D_x')^2]$ , integral over the dipoles.

6304 Common expressions for the calculation of the energy loss and equilibrium quantities,  
6305 in the hypothesis of an isomagnetic lattice, are recalled in Tab. 9.1.

6306 Vertical emittance results from coupling, always present in a ring, due for instance  
6307 to a loss of median plane symmetry, or to fringe fields, or excited on purpose to control  
6308 the vertical emittance as in light sources. Given the coupling factor  $\kappa$  - normally  
6309  $< 0.1$ , the vertical and horizontal emittances satisfy

$$\epsilon_y = \kappa \epsilon_x, \quad \epsilon_x + \epsilon_y = \epsilon_0 \tag{9.48}$$

6310 where  $\epsilon_0$  is the equilibrium horizontal emittance in the absence of coupling (Tab. 9.1).

6311 The basic considerations above hold for a defect-free planar ring. Things can be  
6312 (as usual) more complicated, for instance in the presence of vertical dispersion.

6313 *Field scaling*

6314 Particle stiffness decrease upon SR loss causes these to experience increased field  
 6315 strength ( $1/\rho$  in dipoles,  $G/B\rho$  in quadrupoles, etc.). In the case of beam lines (which  
 6316 may include high energy ERLs [11]), this effect may be taken care of by scaling the  
 6317 magnetic fields to the theoretical average energy loss (Eq. 5.12), namely

$$\Delta E_{scaling} = \sum_{bends} \frac{2}{3} r_0 e c \gamma^3 B \Delta\theta \quad (9.49)$$

6318 In a storage ring the energy lost by SR is restored by the RF system, bends and lenses  
 6319 are operated at constant field. In pulsed regime such as in a booster injector, bends  
 6320 and lenses are operated at constant strength during acceleration.

6321 **9.2.6 Visible Synchrotron Radiation. Interference**

6322 Visible SR was first observed at the GEC 70 MeV. For this reason it has been  
 6323 introduced in the Weak Focusing Synchrotron chapter, Sect. 8.2.3. The SR spectrum  
 6324 at that energy peaks - has its critical frequency - in the visible region. The matter  
 6325 is developed further in the present chapter, in regard with the use of visible SR for  
 6326 beam diagnostics in electron and high energy proton rings [31, 33].

6327 An example of the use of visible SR from a proton beam is found at the CERN SPS,  
 6328 where edge radiation was used at 270 GeV for beam imaging [34]. At that energy  
 6329 in the SPS, the critical frequency (the peak brightness) is in the infrared region.  
 6330 Undulator radiation, more intense, was used down to 200 GeV [35], in the  $p - \bar{p}$   
 6331 collider era (1980s). Another example is the LHC synchrotron light profile monitor,  
 6332 a major beam monitoring tool at injection energy, 450 GeV [36][37, Appendix C].

6333 An example of the use of visible SR from a high energy electron beam is found  
 6334 at the former LEP, where it was produced in a dedicated 4-dipole miniwiggler. The  
 6335 critical frequency in a high energy electron ring is way above the visible range.  
 6336 In such case, visible SR can be dealt with in terms of low-frequency SR [38], a  
 6337 method which can be extended to the analytical treatment of SR interference [37].  
 6338 The underlying theoretical material is recalled here. It is resorted to in the exercises,  
 6339 to cross check Poynting computation from raytracing (using Eq. 8.36).

6340 *Low frequency SR*

6341 A typical electric field impulse from a LEP miniwiggler dipole, and the resulting  
 6342 spectral brightness, as observed in the laboratory, are displayed in Fig. 9.18. The  
 6343 LEP 4-dipole miniwiggler was subject to visible light interference from 4 coherent  
 6344 sources, the effect is illustrated in Fig. 9.19.



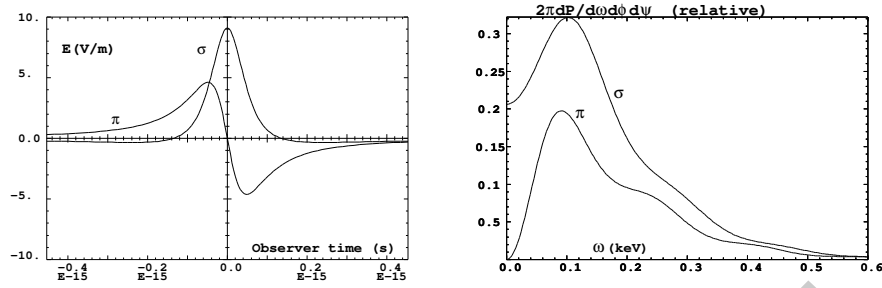


**Fig. 9.18** Left: typical shape of the  $E_\sigma(\tau)$  and  $E_\pi(t)$  electric impulse components of the Poynting vector, emitted by a 2.5 GeV electron on a  $\rho = 53.6$  m circular trajectory in a  $l = 20$  cm-long dipole, as observed in the laboratory.  $E_\sigma, \pi(\tau)$  are obtained from the stepwise integration of electron motion through the magnet, which provides the ingredients to compute Eq. 8.36, accounting for the retarded time  $t = \tau - r(t)/c$  (Eq. 8.37). Right: the spectral brightness of the  $\sigma$  component of the radiation allows comfortable beam diagnostics conditions in the visible range ( $\omega \sim 0.5$  eV)

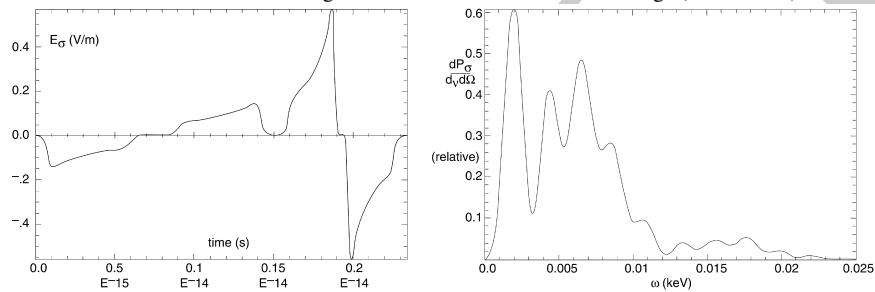


**Fig. 9.19** An interferential spectrum, case of LEP 4-dipole miniwiggler [39]. By contrast with the single dipole case (Fig. 9.18), the spectral brightness of the  $\sigma$  component cancels in the low energy end of the spectrum

6345 A doublet of LEP miniwiggler dipoles, in both cases of same sign and opposite  
 6346 sign dipoles, is the object of numerical simulations in exercise 9.6. It is on the other  
 6347 hand treated theoretically in [37, Sect. 3.1]. The latter provides all necessary material  
 6348 for cross checks of numerical outcomes from the stepwise integration of electron  
 6349 motion,

### 6350 9.2.7 Polarization, Resonances

6351 In a weak focusing optics lattice, radial field components experienced by a particle in  
 6352 the course of its vertical betatron motion are small, which results in weak depolarizing  
 6353 resonances (Sect. 8.2.4). By contrast, strong focusing field gradients in the combined  
 6354 function dipoles and/or focusing lenses of strong focusing optics results in strong  
 6355 radial field components and therefore strong depolarizing resonances.

Spin precession and resonant spin motion in the magnetic components of a cyclic accelerator have been introduced in Sects. 3.2.5, 4.2.5. The general conditions for depolarizing resonance to occur have been introduced in Sect. 8.2.4. In a strong focusing synchrotron they essentially result from the radial field components in the focusing magnets and their strength is determined by the lattice optics, as follows.

### Strength of imperfection resonances

Imperfection, or integer, depolarizing resonances are driven by a non-vanishing vertical closed orbit  $y_{co}(\theta)$  which causes spins to experience periodic radial fields in focusing magnets, dipoles in combined function lattices and quadrupoles in separated function lattices, namely,

$$B_x(\theta) = G y(\theta) = K(\theta) \times B_0 \rho_0 \times y_{co}(\theta) \quad (9.50)$$

with  $\theta$  the orbital angle and  $B_0 \rho_0$  the lattice rigidity. Resonance occurs if the spin undergoes an integer number of precessions over a turn: it then experiences 1-turn-periodic torques, which cause it to move away from the stable  $\mathbf{n}_0$  direction as field perturbations along the closed orbit add up coherently. Thus resonances occur at integer values

$$G\gamma_n = n$$

A Fourier development of these perturbative fields yields the strength of the  $G\gamma_n$  harmonic [40, Sect. 2.3.5.1]

$$\epsilon_n^{\text{imp}} = (1 + G\gamma) \frac{R}{2\pi} \oint K(\theta) y_{co}(\theta) e^{-jG\gamma(\theta - \alpha)} e^{jn\theta} d\theta$$

In the thin-lens approximation, near the resonance where  $G\gamma - n \rightarrow 0$ , this simplifies into a series over the quadrupole fields,

$$\epsilon_n^{\text{imp}} = \frac{1 + G\gamma_n}{2\pi} \sum_{\text{Qpoles}} [\cos G\gamma_n \alpha_i + \sin G\gamma_n \alpha_i] (KL)_i y_{co}(\theta_i) \quad (9.51)$$

with  $\theta_i$  the quadrupole location,  $(KL)_i$  the integrated strength (slice the dipoles as necessary in an AG lattice for this series to converge) and  $\alpha_i$  the cumulated orbit deviation.

Orbit harmonics near the betatron tune ( $n = G\gamma_n \approx \nu_y$ ) excite strong resonances. Imperfection resonance strength is further amplified in P-superperiodic rings, with m-cell superperiods, if the betatron tune  $\nu_y \approx \text{integer} \times m \times P$  [41, Chap.3-I].

### Strength of intrinsic resonances

6375 Intrinsic depolarizing resonances are driven by betatron motion, which causes spins  
6376 to experience strong radial field components in quadrupoles, namely

$$B_x(\theta) = G y(\theta) = K(\theta) \times B_0 \rho_0 \times y_\beta(\theta) \quad (9.52)$$

The effect of resonances on spin depends upon betatron amplitude and phase, their effect on beam polarization depends on beam emittance. Longitudinal fields from dipole ends are usually weak by comparison and ignored. The location of intrinsic resonances depends on betatron tune, it is given in an M-periodic structure by

$$G\gamma_n = nM \pm \nu_y$$

A Fourier development of the perturbative fields yields the two families of strengths [40, Sect. 2.3.5.2]

$$\epsilon_n^{\text{intr}\pm} = \frac{\lambda_x \rho_0}{4\pi} \int_0^{2\pi} K(\theta) \sqrt{\beta_y(\theta)} \frac{\epsilon_y}{\pi} e^{\pm j \left( \int_0^{s(\theta)} \frac{ds}{\beta_y} - \nu_y \theta \right)} e^{-jG\gamma(\theta - \alpha(\theta))} e^{jn\theta} d\theta$$

6377 In the thin-lens approximation, near the resonance where  $G\gamma \pm \nu_y - n \rightarrow 0$ , this  
6378 simplifies into a series over the quadrupole fields,

$$\left\{ \begin{array}{l} \mathcal{R}e(\epsilon_n^{\text{intr}\pm}) \\ j \mathcal{I}m(\epsilon_n^{\text{intr}\pm}) \end{array} \right\} = \frac{1 + G\gamma_n}{4\pi} \sum_{\text{Qpoles}} \left\{ \begin{array}{l} \cos(G\gamma_n \alpha_i \pm \varphi_i) \\ j \sin(G\gamma_n \alpha_i \pm \varphi_i) \end{array} \right\} (KL)_i \sqrt{\beta_{y,i}} \frac{\epsilon_y}{\pi} \quad (9.53)$$

### 6379 Spin diffusion

6380 Spin diffusion stems from the stochastic emission of photons in magnetic fields  
6381 (Sect. 5.2.3.1). A change  $\delta$  in the energy offset  $\Delta E$  of a particle, due to the emission of  
6382 a photon, causes a change  $\partial \mathbf{n} / \partial \delta$  of the local spin precession direction. In dispersive  
6383 sections it also causes a change in the horizontal invariant,  $\partial \epsilon_x / \partial \delta$ , and in vertical  
6384 invariant as well,  $\partial \epsilon_y / \partial \delta$  in the presence of vertical dispersion, which in turn result  
6385 in perturbations  $\partial \mathbf{n} / \partial \epsilon_{x,y}$ .

6386 As far as numerical integration is concerned, spin diffusion is a sub-product of the  
6387 stepwise integration of Thomas-BMT equation (Sect. 3.2.5), and of the simulation of  
6388 stochastic emission of photons (Sect. 5.2.3.1). It is at work in Cornell RCS simulation,  
6389 exercise 9.4.

## 6390 9.3 Exercises

6391 In complement to the present exercises, a tutorial on depolarizing resonances in  
6392 a strong focusing synchrotron can be found in [40, Chap. 14]. Proton, helion and  
6393 electron beams are considered, using the lattice of the AGS Booster at BNL. The

6394 simulations explore methods for preservation of polarization, including tune-jump  
 6395 quadrupoles, a solenoid, Siberian snakes, spin rotators in the case of electrons,  
 6396 including synchrotron radiation and effects on polarization life time.

6397 Note: input data files for these simulations are available in zgoubi sourceforge  
 6398 repository at

6399 [https://sourceforge.net/p/zgoubi/code/HEAD/tree/branches/exemples/book/zgoubiMaterial/synchrotron\\_strongFocusing/](https://sourceforge.net/p/zgoubi/code/HEAD/tree/branches/exemples/book/zgoubiMaterial/synchrotron_strongFocusing/)

## 6400 9.1 Construct SATURNE 2 Synchrotron

6401 Solution: page 340

6402 Over the years 1978-1997 the 3 GeV synchrotron SATURNE 2 at Saclay (Figs. 9.3, 9.20)  
 6403 delivered polarized proton beams, and polarized deuteron and  ${}^6\text{Li}$  beams up to  
 6404 1.1 GeV/nucleon, for intermediate energy nuclear physics research, including meson  
 6405 production [45, 42, 43]. The separated function synchrotron was designed *ab initio*  
 6406 for the acceleration of polarized ion beams [44], and the first strong focusing syn-  
 6407 chrotron to do so - ZGS, first to accelerate polarized beams, protons and deuterons,  
 6408 was a weak focusing synchrotron (Chap. 8).

6409 SATURNE 2 is a FODO lattice with missing dipole. Its parameters are given in  
 6410 Tab. 9.2.

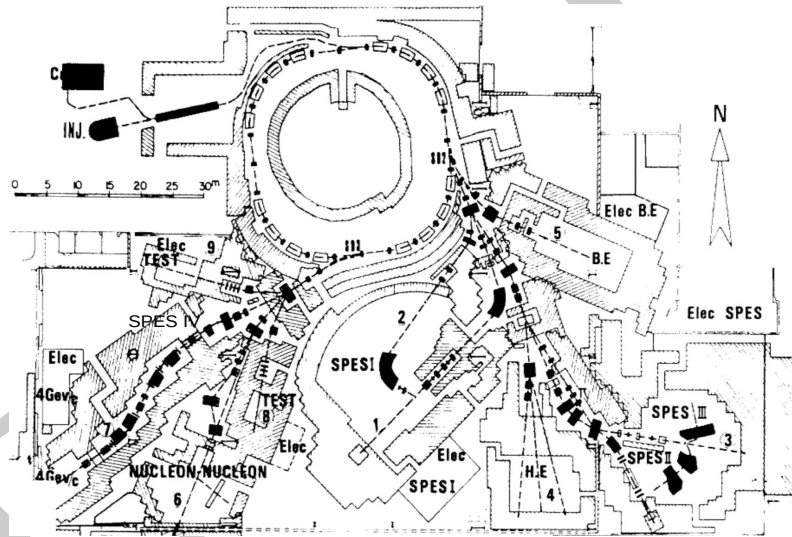


**Fig. 9.20** SATURNE 2 synchrotron and its experimental areas, including mass spectrometers SPES I to SPES IV, a typical nuclear physics accelerator facility. The polarized ion sources Dioné and Hypérian are at the top left, followed by a 20 MeV linac. In the early 1980s a synchrotron booster, MIMAS, was added for higher polarized ion performance

(a) Simulate the main dipole using BEND. Dipole fringe fields matter in this small ring, take them into account assuming  $\lambda = 8$  cm extent and the following Enge coefficient values (Eq. 14.11, Sect. 14.3.3):

**Table 9.2** Parameters of SATURNE2 separated function FODO lattice.  $\rho_0$  is the radius of the reference orbit in the main dipole

Orbit length, $C$	m	105.5556
Average radius, $R = C/2\pi$	m	16.8
Straight sections, length:		
- short	m	0.716256
- long	m	3.92148
Dipole:		
- bend angle, $\alpha$	deg	22.5
- magnetic radius, $\rho_0$	m	6.3381
- wedge angle, $\varepsilon$	deg	2.45
Quadrupole:		
- gradient range	T/m	0.5 - 10.56
- magnetic length F/D	m	0.46723 / 0.486273
Wave numbers, typical, $\nu_x; \nu_y$		3.64; 3.60
Chromaticities, $\xi_x; \xi_y$		negative, a few units
Momentum compaction $\alpha$		0.015
Injection energy (proton)	MeV	20
Top energy	GeV	3
$\dot{B}$	T/s	4.2
Synchronous energy gain	keV/turn	1.160
RF harmonic		2

$$C_0 = 0.2401, C_1 = 1.8639, C_2 = -0.5572, C_3 = 0.3904, C_4 = C_5 = 0$$

6411 Produce the transport matrix of the dipole, check against theory. Compare with  
6412 the matrix of the hard edge model.

6413 Produce a graph of the field across the dipole, in the median plane and at 5 cm ver-  
6414 tical distance. OPTIONS[CONSTY=ON] can be used to force a particle to constant  
6415 Y and Z.

6416 Simulate the F and D quadrupoles, using respectively QUADRUPOLE and MUL-  
6417 TIPOL. Compare matrices with theory.

6418 Construct the cell. Produce machine parameters (tunes, chromaticities), check  
6419 against data, Tab. 9.2.

6420 Construct the 4-cell ring. Produce a graph of the optical functions. Produce the  
6421 beam matrix.

6422 (b) Accelerate a bunch comprised of a few tens of particles with Gaussian density  
6423 distributions (it can be defined using MCOBJET), from injection to top energy,  
6424 50 MeV to 3 GeV. Use harmonic 3 RF frequency, take a (unrealistic, for a reduced  
6425 number of turns) peak RF voltage  $\hat{V} = 1$  MV, and synchronous phase  $\phi_s = 30$  deg.

6426 Produce a graph of Y, Z and dp/p versus turn. Check the transverse damping  
6427 against theory.

6428 (c) Determine the momentum acceptance of the ring at 50 MeV, with  $\hat{V} = 10$  kV  
6429 peak voltage, in the following four cases: stationary bucket (synchronous phase  
6430  $\phi_s = 0$ ) and accelerated buckets with  $\phi_s = 15, 30,$  and  $60$  deg.

6431 Reproduce the longitudinal phase space graphs displayed in Fig. 9.16.

## 6432 9.2 Non-Linear Motion in SATURNE 2

6433 Solution: page 348

6434 (a) Simulate horizontal particle motion near a third integer resonance. Provide a  
6435 graph of the transverse phase space.

6436 (b) Simulate horizontal particle motion near a quarter integer resonance. Provide  
6437 a graph of the transverse phase space.

### 6438 9.3 SVD Orbit Correction

6439 Solution: page 351

6440 Using SATURNE 2 ring, inject dipole defects and use SVDOC to find the cor-  
6441 rected orbit.

6442 It can be done in the following way:

6443 - place a horizontal pickup (HPU), a dipole defect (HDEF, using a thin-lens  
6444 MULTIPOL, length *e.g.* 1e-3 cm) and a dipole corrector (HKIC, using a thin-lens  
6445 MULTIPOL) in the middle of the QF quadrupole of the FODO cells,

6446 - in a similar manner, place a VPU, a VDEF and a VKIC just upstream of the  
6447 FODO cell QD,

6448 - excite V and H closed orbits by injecting random defects in HKIC and VKIC,  
6449 using ERRORS.

6450 Use SVDOC to find the orbit correction.

6451 Provide a graph of the orbit at the PUs, before and after correction.

6452 In the previous setting, there is 24 defects (12 H and 12 V) and 24 correctors (12  
6453 H and 12 V). Repeat for 24 defects and only 12 correctors per plane.

### 6454 9.4 Cornell Electron RCS. Radiative Energy Loss

6455 Solution: page 353

6456 Note: details regarding these simulations and their solutions can be found in the  
6457 Tech. Note EIC/57;BNL-114452-2017-IR [46].

6458 The goal in this exercise is to simulate Cornell RCS lattice and accelerate beam,  
6459 first without synchrotron radiation, then taking it into account. In a fourth step  
6460 electron spin is added and polarization transmission through the acceleration cycle  
6461 assessed.

6462 (a) Details of the RCS geometry and lattice can be found in Ref. [14], however a  
6463 simplified 6-superperiodic version of the ring is considered here, with six identical  
6464 long straights and six identical arcs. The RCS parameters are given in Tab. 9.3. The  
6465 input data files are given in

6466 - Tabs. 9.4 and 9.5: definition of the focusing and defocusing bends, and of the  
6467 focusing and defocusing doublets;

6468 - Tab. 9.6: definition of a FODO cell;

6469 - Tab. 9.7: definition of a supercell;

6470 - Tab. 9.8: definition of the 6-supercell ring.

6471 Produce the optical parameters of the ring. A TWISS command can be used for  
6472 that. Produce graphs of the closed orbit and optical functions around the ring.

6473 (b) Raytrace a few tens of particles over 2300 turns around the ring, from 320 MeV  
6474 to 8 GeV about, ignoring radiative energy loss. Assume normalized emittances  $\epsilon_x =$

**Table 9.3** Cornell RCS parameters in the present simplified lattice simulation

Top energy	GeV	7
Injection energy	MeV	320
Circumference, simplified 6-supercell case	m	786.947
<i>Bunch</i>		
$\varepsilon_x, \varepsilon_y$ at injection	$\pi\mu\text{m}$	25
Bunch length	mm	6
dE/E at injection		$5 \cdot 10^{-3}$
<i>Combined function lattice</i>		
Nb of F and D cell dipoles		48×FFDD 192
$\rho_F, \rho_D$	m	≈95, 92
Field at 7 GeV	T	0.25
Max. $\beta_x, \beta_y$	m	29, 26
$\nu_x, \nu_y$ , natural		9.62, 13.82
$\xi_x, \xi_y$ , natural		-13, -16
<i>RF, synch. radiation</i>		
Repetition rate	Hz	up to 60
Acceleration rate	MV/turn	3
E-loss per turn at 5, 10 GeV	MeV	0.6, 9
$\tau_x (\approx \frac{2.5}{E^3})$ at 5, 10 GeV	ms	16, 2

6475  $\varepsilon_y = 25\pi\mu\text{m}$ , Gaussian densities, initial *rms*  $\delta p/p = 5 \cdot 10^{-3}$ . Use CAVITE[IOPT=3]  
 6476 for acceleration. Produce a graph of the three phase spaces. produce graphs of  
 6477 transverse and longitudinal excursions versus turn number, check damping again  
 6478 expectations.

6479 (c) Re-do (b) with synchrotron radiation energy loss, following SR loss theoret-  
 6480 ical material introduced in the “Betatron” Chap. 5. Use SRLOSS for radiation, and  
 6481 CAVITE[IOPT=11, Facility=CornellSynch,  $U_{00} = 9.48145321 \times 10^{-6}$ ] for accelera-  
 6482 tion. Check equilibrium emittances.

6483 (d) Produce a graph of the average bunch polarization over the acceleration cycle  
 6484 in (c), starting with all spins up at injection energy. Check against the resonance  
 6485 spectrum over  $a\gamma : 0.7 \rightarrow 18$ .

**Table 9.4** Simulation input data files for the focusing (left) and defocusing (right) combined function dipoles. They define the segments, respectively, F\_BEND\_S:F\_BEND\_E and D\_BEND\_S:D\_BEND\_E, for use by INCLUDE commands in further input data files. These files can be run as is: FIT will center the closed orbit across the magnet, accounting for the field scaling by the *ad hoc* coefficient under SCALING

```

RCS focusing combined function dipole
! File: F_BEND.inc
'OBJET'
1. *1e3
5
.001 .001 .001 .001 0. .0001
0. 0. 0. 0. 0. 1.

'SCALING'
1 1
MULTIPOL F_BEND
-1
0.98523998
1

'MARKER' F_BEND_S

'MULTIPOL' F_BEND
0 .Dip
320.2700 10. 0.1021746 0.0435214 0. 0. 0. 0. 0. 0. 0.
0. 0. 10.00 4.0 0.800 0.00 0.00 0.00 0.00 0. 0. 0.
4 .1455 2.2670 -.6395 1.1558 0. 0. 0.
0. 0. 10.00 4.0 0.800 0.00 0.00 0.00 0.00 0. 0. 0.
4 .1455 2.2670 -.6395 1.1558 0. 0. 0.
0. 0. 0. 0. 0. 0. 0. 0. 0. 0.
#30|320|30 ! YCE offset found by FIT
3 0.0000000000E+00 0.52818473 -1.6362461735E-02

'MARKER' F_BEND_E

'FIT'
1
4 65 0 [-.4,.4.]
2
3.1 1 2 #End 0. 1. 0
3.1 1 3 #End 0. 1. 0

'END'

RCS defocusing combined function dipole
! File: D_BEND.inc
'OBJET'
1. *1e3
5
.001 .001 .001 .001 0. .0001
0. 0. 0. 0. 0. 1.

'SCALING'
1 1
MULTIPOL D_BEND
-1
1.1078694
1

'MARKER' D_BEND_S

'MULTIPOL' D_BEND
0 .Dip
320.0150 10. 0.1022560 -0.0437325 0. 0. 0. 0. 0. 0. 0.
0. 0. 10.00 4.0 0.800 0.00 0.00 0.00 0.00 0. 0. 0.
4 .1455 2.2670 -.6395 1.1558 0. 0. 0.
0. 0. 10.00 4.0 0.800 0.00 0.00 0.00 0.00 0. 0. 0.
4 .1455 2.2670 -.6395 1.1558 0. 0. 0.
0. 0. 0. 0. 0. 0. 0. 0. 0. 0.
#30|320|30 ! YCE offset found by FIT
3 0.0000000000E+00 -1.4110319 -1.6362461735E-02

'MARKER' D_BEND_E

'FIT'
1
4 65 0 [-.2,.2.]
2
3.1 1 2 #End 0. 1. 0
3.1 1 3 #End 0. 1. 0

'END'

```

**Table 9.5** definition of focusing (left) and defocusing (right) doublets, for use by further INCLUDE commands

```

! File: BF2.inc
'MARKER' BF2_S
'DRIFT'
23.999061
'INCLUDE'
1
F_BEND.inc[F_BEND_S:F_BEND_E]
'DRIFT'
23.999061
'DRIFT'
23.999061
'INCLUDE'
1
F_BEND.inc[F_BEND_S:F_BEND_E]
'DRIFT'
23.999061

'MARKER' BF2_E
'END'

! File: BD2.inc
'MARKER' BD2_S
'DRIFT'
24.126561
'INCLUDE'
1
D_BEND.inc[D_BEND_S:D_BEND_E]
'DRIFT'
24.126561
'DRIFT'
24.126561
'INCLUDE'
1
D_BEND.inc[D_BEND_S:D_BEND_E]
'DRIFT'
24.126561

'MARKER' BD2_E
'END'

```

**Table 9.6** Simulation input data file for a FODO cell

```

! File: FD.inc
'MARKER' FD_S
'INCLUDE'
1
BF2.inc[BF2_S:BF2_E]
'INCLUDE'
1
BD2.inc[BD2_S:BD2_E]
'MARKER' FD_E
'END'

```



**Table 9.7** Simulation input data file for a supercell

```

File : superCell.inc
'OBJET'
1. *1e3          ! Rigidity is 1 T m.
5
.001 .001 .001 .001 0. .0001
0. 0. 0. 0. 0. 1.

'MARKER' superCell_S

'INCLUDE'
1
F_BEND.inc[F_BEND_S:F_BEND_E]
'DRIFT'
40.988209
'DRIFT'
40.988209
'INCLUDE'
1
F_BEND.inc[F_BEND_S:F_BEND_E]
'DRIFT'
15.600113
'DRIFT'
15.600113
'INCLUDE'
1
D_BEND.inc[D_BEND_S:D_BEND_E]
'DRIFT'
24.062811
'DRIFT'
24.062811
'INCLUDE'
1
D_BEND.inc[D_BEND_S:D_BEND_E]
'DRIFT'
15.600113
'DRIFT'
15.600113
'INCLUDE'
1
F_BEND.inc[F_BEND_S:F_BEND_E]
'DRIFT'
40.988209
'DRIFT'
40.988209
'INCLUDE'
1
F_BEND.inc[F_BEND_S:F_BEND_E]
'DRIFT'
15.600113
'INCLUDE'
1
D_BEND.inc[D_BEND_S:D_BEND_E]
'DRIFT'
15.600113
'DRIFT'
15.600113
'INCLUDE'
1
D_BEND.inc[D_BEND_S:D_BEND_E]
'DRIFT'
40.988209
'DRIFT'
40.988209
'INCLUDE'
1
F_BEND.inc[F_BEND_S:F_BEND_E]
'DRIFT'
15.600113
'DRIFT'
15.600113
'INCLUDE'
1
F_BEND.inc[F_BEND_S:F_BEND_E]
'DRIFT'
24.062811
'INCLUDE'
1
BD2.inc[BD2_S:BD2_E]

'DRIFT'
24.062811
'MULTIPOL'
0 .Dip
44.6375 10. 0.1022198 -0.0437325 0. 0.0 0.0 0.0 0.0 0.0 0.0 0.0
0. 0. 10.00 4.0 0.800 0.00 0.00 0.00 0.00 0.0 0. 0. 0.
4 .1455 2.2670 -.6395 1.1558 0. 0. 0.
0. 0. 10.00 4.0 0.800 0.00 0.00 0.00 0.00 0.0 0. 0. 0.
4 .1455 2.2670 -.6395 1.1558 0. 0. 0.
0. 0. 0. 0. 0. 0. 0. 0. 0. 0.
#30|45|30 Dip B129VA
3 0.00000000000E+00 1.77777778E-02 -2.2814180400E-03
'MULTIPOL'
0 .Dip
275.505 10. 0.1022165 0.0842350 0. 0.0 0.0 0.0 0.0 0.0 0.0 0.0
0. 0. 10.00 4.0 0.800 0.00 0.00 0.00 0.00 0.0 0. 0. 0.
4 .1455 2.2670 -.6395 1.1558 0. 0. 0.
0. 0. 10.00 4.0 0.800 0.00 0.00 0.00 0.00 0.0 0. 0. 0.
4 .1455 2.2670 -.6395 1.1558 0. 0. 0.
0. 0. 0. 0. 0. 0. 0. 0. 0. 0.
#30|276|30 Dip B129HB
3 0.00000000000E+00 0.65358025 -1.4081043695E-02
'DRIFT'
24.062811
'DRIFT'
60.800000
'DRIFT'
244.000000
'DRIFT'
244.000000
'DRIFT'
60.800000
'DRIFT'
24.062811
'MULTIPOL'
0 .Dip
275.505 10. 0.1022165 -0.0844460 0. 0.0 0.0 0.0 0.0 0.0 0.0 0.0
0. 0. 10.00 4.0 0.800 0.00 0.00 0.00 0.00 0.0 0. 0. 0.
4 .1455 2.2670 -.6395 1.1558 0. 0. 0.
0. 0. 10.00 4.0 0.800 0.00 0.00 0.00 0.00 0.0 0. 0. 0.
4 .1455 2.2670 -.6395 1.1558 0. 0. 0.
0. 0. 0. 0. 0. 0. 0. 0. 0. 0.
#30|276|30 Dip B128VA
3 0.00000000000E+00 0.6397805 -1.4081043695E-02
'MULTIPOL'
0 .Dip
44.6375 10. 0.1022198 0.0435214 0. 0.0 0.0 0.0 0.0 0.0 0.0 0.0
0. 0. 10.00 4.0 0.800 0.00 0.00 0.00 0.00 0.0 0. 0. 0.
4 .1455 2.2670 -.6395 1.1558 0. 0. 0.
0. 0. 10.00 4.0 0.800 0.00 0.00 0.00 0.00 0.0 0. 0. 0.
4 .1455 2.2670 -.6395 1.1558 0. 0. 0.
0. 0. 0. 0. 0. 0. 0. 0. 0. 0.
#30|45|30 Dip B128HB
3 0.00000000000E+00 1.77777778E-02 -2.2814180400E-03
'DRIFT'
24.062811
'INCLUDE'
1
5 * FD.inc[FD_S:FD_E]
'DRIFT'
7.073665 ! -24.126561 + 2*15.600113
'MARKER' superCell_E

'TWISS'
2 1. 1.

'SYSTEM'
1
gnuplot <./gnuplot_TWISS.gnu

'END'

```

**Table 9.8** Simulation input data file for Cornell RCS ring

```

File: ring.INC.dat. Cornell RCS ring
'OBJECT'
1. *1e3
5
.001 .001 .001 .001 0. .0001
0. 0. 0. 0. 0. 1.

'OPTIONS'
1 1
WRITE OFF

'SCALING'
1 3
MULTIPOL
-1
1.
1
MULTIPOL_F_BEND
-1
0.99292280
1
MULTIPOL_D_BEND
-1
1.1294084
1

'INCLUDE'
1
6 * superCell.inc[superCell_S:superCell_E]

'OPTIONS'
1 1
WRITE ON

!'TWISS'          ! Uncomment to get a TWISS and graphs.
!2 1. 1.
!'SYSTEM'
!1
!gnuplot <./gnuplot_TWISS.gnu
!'END'

'FIT2' ! Set SCALING coefficients for requested tunes.
2
3 8 0 .2
3 12 0 .2
2
0.1 7 0 #End 0.62 1. 0
0.1 8 0 #End 0.82 1. 0

!'MATRIX'
!1 11
!'TWISS'
2 1. 1.
!'END'

```

**6486 9.5 Coupling in a Light Source Storage Ring**

6487 In this exercise, it is proposed to reproduce SR damping simulations, in a case of  
6488 coupled light source lattice, detailed in JINST article [48]

6489 *Simulation of radiation damping in rings, using stepwise ray-tracing methods*  
6490 (the original (1990s) ESRF lattice is concerned - today's ESRF lattice is completely  
6491 different, minimal emittance, un-isomagnetic).

6492 An input data file for the early ESRF lattice can be found at

6493 [https://sourceforge.net/p/zgoubi/code/HEAD/tree/  
6494 branches/exemples/SRDamping/ESRFRing/coupled](https://sourceforge.net/p/zgoubi/code/HEAD/tree/branches/exemples/SRDamping/ESRFRing/coupled)

6495 It accounts for  $\kappa = 0.58$  optical coupling, by a single skew quadrupole placed at the  
6496 beginning of the lattice.

6497 Reproduce the numerical results for this coupled case, as detailed in Sect. 5 of  
6498 that JINST article [48].

**6499 9.6 SR Electric Impulse and Interference in a Miniwiggler**

6500 Solution: page 356

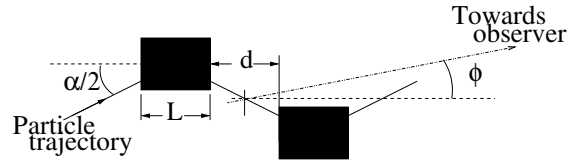
6501 In this exercise, the electric field component of synchrotron radiation in short  
6502 dipoles is produced. An interferential spectrum is produced from a pair of dipoles.  
6503 This exercise is based on the LEP miniwiggler configuration [37].

6504 (a) Produce the input data file for the simulation of an electron trajectory in one of  
6505 the LEP miniwiggler dipoles schemed in Fig. 9.21. Dipole length is  $L = 52.602$  cm,  
6506 bend angle  $0.8$  mrad. Electron energy is  $E = 45$  GeV. Produce the electric field  
6507 impulse observed at long distance in the direction  $\phi = \psi = 0$ . Produce its spectrum.

6508 Check the various quantities: duration of the electric field impulse, critical fre-  
6509 quency of the spectrum, etc.

6510 (b) Consider the dipole pair of 9.21. Take distance between dipoles  $d = 23.098$ .  
6511 Produce the electric field impulse observed at long distance in the direction  $\phi = \psi =$   
6512  $0$ . Produce its spectrum.

**Fig. 9.21** Synchrotron radiation electric field impulse from a pair of dipoles is observed in the direction  $(\phi, \psi)$ , with  $\phi$  the bend plane angle as shown, and  $\psi$  the angle to the bend plane. This schematic defines the observation direction  $\phi = 0$



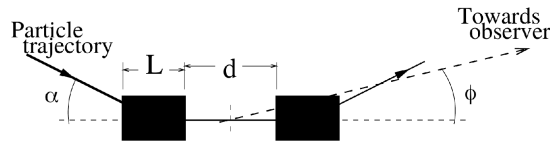
6513 Check the various quantities: duration of the electric field impulse, critical frequency of the spectrum.

6514 Repeat, in the direction  $\phi = 0$ ,  $\psi = 0.2$  mrad.

6515 (c) Repeat (b), for the dipole pair disposed as in Fig. 9.21 [37, Sect. A].

6516 (d) Repeat (c) for the configuration of Fig. 9.22, a case of edge radiation interference [37, Sect. B].

**Fig. 9.22** Both dipoles have same sign. This schematic defines the observation direction  $\phi = 0$



6518

## 6519 9.7 Depolarizing Resonances in SATURNE 2

6520 Solution: page 360

6521 Unexpectedly as it is not a systematic resonance,  $G\gamma = 7 - \nu_y$  was found to be harmful to beam polarization. Produce a crossing of that resonance, for a few particles with different momenta, and vertical invariant  $\epsilon_z \approx 10\pi\mu\text{m}$ . Take peak voltage 6 kV and synchronous phase  $\phi_s = 0.2363176$  rad.

6525 The input data file given in Tab. 9.14, an outcome of exercise 9.15, can be used as a starting point for this simulation.

## 6527 9.8 Ion and Electron Polarization. Preservation of Polarization

6528 More simulations regarding

6529 - spin polarized ions and special devices and methods for the preservation of polarization during acceleration, including tune jump, partial and full Siberian snakes, etc.,

6532 - electron spin diffusion in a storage ring and its suppression, spin matching, polarization lifetime, etc.,

6534 can be found, with complete solutions, in the USPAS Summer 2021 Spin Class Lectures, "Polarized Beam Dynamics and Instrumentation in Particle Accelerators" [47, Chap. 14].

6536